ChemComm

COMMUNICATION

High Resolution Visualization of the Redox Activity of Li_2O_2 in Non-Aqueous Media: Conformal Layer vs. Toroid Structure

Received 00th December 2017,
Accepted 00th December 2017

DOI: 10.1039/x0xx00000x

www.rsc.org/

Sharel P. E,[ab] Minkyung Kang,[a] Paul Wilson,[a] Lingcong Meng,[a] David Perry,[a] Andrew Basile,*[ac] and Patrick R. Unwin*[a]

A strong relationship between surface structure and the redox activity of Li_2O_2 is visualized directly with scanning electrochemical cell microscopy, employing a dual-barrel nanopipette containing a unique gel polymer electrolyte. These measurements reveal considerable local heterogeneity with significantly enhanced electrochemical activity at toroidal Li_2O_2 structures when compared to the conformal layer that is usually formed on the cathode of Li-O_2 batteries.

Lithium-oxygen (Li-O_2) batteries are envisioned to be a key enabling technology for future electric transportation and energy storage systems, due to the high specific energy that is potentially realizable from these devices.[1-4] However, practical Li-O_2 cells are presently suboptimal and formidable scientific and technical challenges need to be overcome,[5-7] including improvements to cycle life, addressing capacity fading and decreasing the large overpotential during recharge. These problems are mostly related to passivation of the cathode during the discharge process, a result of the build-up of a wide bandgap insulating layer of Li_2O_2.[8-9] A plethora of methods have been used to investigate the structure of Li_2O_2 and elucidate the mechanism of formation, including several microscopic, electrochemical and spectroscopic techniques.[10-13] It has been suggested that the charge-discharge capacity can be increased if Li_2O_2 forms as toroidal particles as opposed to the more typical thin conformal layer.[14-17] Atomic force microscopy (AFM), in tandem with spectroscopy, was recently used to investigate topographical changes during the formation and electro-dissolution of toroidal Li_2O_2 on a gold substrate.[18]

In this study, we implement electrochemical mapping that allows direct comparison of the behavior of the conformal layer and toroidal structures in isolation, but on the same electrode. This is achieved through the use of scanning electrochemical cell microscopy (SECCM), in a controlled atmospheric environment, in tandem with field emission-scanning electron microscopy (FE-SEM), *applied to the same area*, and complementary AFM and micro-Raman spectroscopy measurements. This approach provides a holistic view of structural controls of Li_2O_2 electroactivity and the results obtained guide the development of optimal Li_2O_2 structures.

Gold substrates for Li_2O_2 formation were prepared by evaporating Cr (3 nm) followed by Au (60 nm) using a Moorfields MiniLab deposition system. Rather than carbon, a gold electrode was chosen to prevent Li_2CO_3 formation at the cathode via carbon decomposition.[19-20] The Li_2O_2 surface was prepared by driving the oxygen reduction reaction (ORR). The potential was held at 1.87 V_{Li/Li^+} for 10 s in order to achieve the required current density on these smooth gold surfaces. This was achieved using O_2 saturated 0.1 M $LiClO_4$ dimethyl sulfoxide (DMSO) (details in S1, Fig. S1, ESI†) to drive the following reaction:[18, 21]

$$2Li^+ + 2e^- + O_2 \leftrightharpoons Li_2O_2 \quad (1)$$

As shown in the FE-SEM image in Fig. 1a, under the experimental conditions, Li_2O_2 toroids (1 – 1.5 µm in diameter) form atop the uniform thin Li_2O_2 layer, with a coverage of about one particle per 20 µm². An FE-SEM image of a Li_2O_2 toroid at higher magnification (inset) shows a nanocrystalline, aggregated structure, likely grown at defect sites in the otherwise homogeneous Li_2O_2 film.[17] The micro-Raman spectrum (Fig. 1b), over the range 460 to 1040 cm^{-1} on a single Li_2O_2 toroid, confirmed the presence of Li_2O_2, with a peak at 805 cm^{-1} which is attributed to the O–O stretch of Li_2O_2.[22-24] An AFM image in Fig. 1c displays four Li_2O_2 toroids, with a magnified image of one of the toroids (Fig. 1d) in agreement with the FE-SEM data, showing an aggregated morphology, made up from numerous nanoscale Li_2O_2 particles. In contrast, Fig. 1e shows the relatively homogenous conformal Li_2O_2 layer on the gold substrate. The line profile in Fig. 1f shows the toroid structures exhibit diameters in the range 1.2 – 2.0 µm and are 0.5 – 1.1 µm

[a]Department of Chemistry, University of Warwick, Gibbet Hill Road, Coventry, UK
[b]Department of Chemical Engineering & Biotechnology, University of Cambridge, CB3 0AS Cambridge, UK
[c]Institute for Frontier Materials (IFM), Deakin University, Burwood, Victoria 3125, Australia.
*To whom correspondence should be addressed. E-mail: andrew.basile@deakin.edu.au , p.r.unwin@warwick.ac.uk
†Electronic Supplementary Information (ESI) available: [Experimental details, and Fig. S1-S2, Movie S1-S2 mentioned in the text.]. See DOI: 10.1039/x0xx00000x

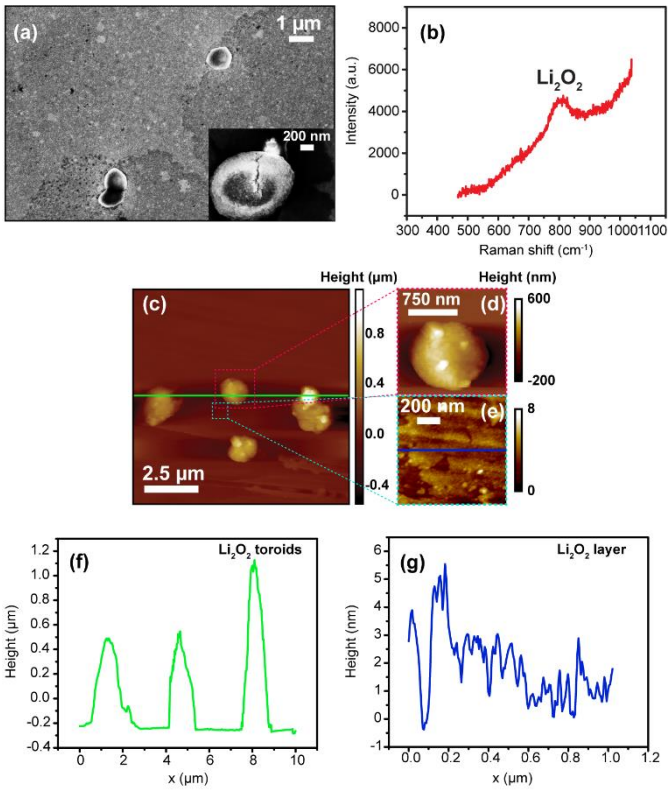

Fig. 1 (a) FE-SEM images after Li_2O_2 growth on a gold substrate electrode (Li_2O_2 toroids on top of thin Li_2O_2 layer); inset shows a toroid at higher magnification. (b) Typical micro-Raman spectrum of a Li_2O_2 toroid. (c) Typical AFM image of Li_2O_2 toroids on a conformal layer, with magnified images of (d) a spherical Li_2O_2 toroid and (e) the Li_2O_2 conformal layer. Corresponding height cross sections across Li_2O_2 toroids (f) and the conformal layer (g). Note the difference in height scale.

in height. The conformal layer of Li_2O_2 has a roughness of just a few nm (Fig. 1g).

Previous studies with SECCM have employed aqueous solutions[25-26] or ionic liquids.[27-28] However, typical organic solvents of low viscosity tend to wet surfaces too well, making the meniscus contact unstable. An important part of this work was therefore to develop a gel polymer DMSO electrolyte probe, trapping the liquid component in a polymer matrix, while maintaining the electrolyte properties.[29-30]

DMSO has been utilized with success in recent studies for high performance rechargeable Li-air batteries.[23, 31, 34] The gel polymer electrolyte formulation allowed the pre-gel solution to flow into the dual-channel nanopipette probes, which had a total tip diameter of *ca.* 140 nm, prior to curing (see Fig. S2, ESI†). To this end, a low molecular weight, poly(glycidyl methacrylate) (PGMA) was synthesized by catalytic chain transfer polymerization. Using this technique the molecular weight ($M_{n,SEC}$) was limited to 1900 g mol^{-1} equating to an average degree of the polymerization (DP_n) of 12. Thus, the viscosity of the polymer matrix in solution of the 0.1 M tetrabutylammonium hexafluorophosphate ($TBAPF_6$)/DMSO electrolyte remained low, and the pendent epoxide functional group was predisposed for cross-linking using a *bis*-amine reagent (4,7,10-trioxa-1,13-tridecanediamine). To establish optimal gel formulation, the loading of the polymer matrix in the electrolyte (1-10 % *w/w*) and the concentration of cross-linker relative to epoxide groups (1-50 mol%) was varied. A formulation consisting of PGMA (10 % *w/w*), cross-linker (50 mol% with respect to epoxide) and 0.1 M $TBAPF_6$/DMSO was found to have reasonable conductivity of *ca.* 1050 µS cm^{-1}. A Ag/AgCl wire was inserted into each channel of the nanopipette probe, to act as quasi-reference counter electrodes (QRCEs), followed by curing for 8 hours at 80 °C (under Ar). The resultant nanopipette containing organic gel was kept under Ar and transferred rapidly to the SECCM environmental cell (details in the ESI† S1). All potentials were converted to the Li/Li$^+$ scale ($E_{Ag/AgCl}$ = 2.82 V vs. Li/Li$^+$).

SECCM was operated in a hopping cyclic voltammetry (CV) mode (Fig. 2a), whereby the electrochemical cell (nanopipette) was introduced to the surface, to make meniscus contact, without the nanopipette itself touching the surface. The procedures for landing the probe meniscus at a series of locations across the surface of interest, *via* measurement of the conductance current between the 2 channels of the probe (I_{IC}) is described in S1 ESI†. Both I_{IC} and the working electrode current (I_{EC}) were measured using custom-built current-to-voltage converters. The performance of the gel electrolyte under SECCM environmental control conditions was compared to the voltammetric response known for DMSO electrolytes.[32] A typical CV is shown in Fig. 3 and the response is very similar to dry DMSO solution (e.g. Figure 1 in ref. 32) highlighting the suitability of the gel probes, with a wide potential window between the potentials for oxidation and reduction of the electrolyte/solvent.

To probe the behavior of both Li_2O_2 toroids and thin Li_2O_2 film, the hopping distance between each measurement/pixel was 3 µm, both to avoid overlap of the meniscus areas (*ca*. 2.5 µm in diameter, *vide infra*) and cover a wide region. The images herein comprise 240 pixels and at each pixel 2 CVs, each involving the recording of the current as the potential was swept cathodically from 3.12 $\mathbf{V_{Li/Li^+}}$ to 0.22 $\mathbf{V_{Li/Li^+}}$ (negative direction) followed by scanning positively to 4.72 $\mathbf{V_{Li/Li^+}}$ (scan rate of 1 V s^{-1}; potential resolution of 5.12 mV) (Fig. 2b). These data were used to make two electrochemical movies, with each consisting of 900 current images as a function of applied potential (E_{app}); see ESI† Movie S1 (1st cycle) and S2 (2nd cycle).

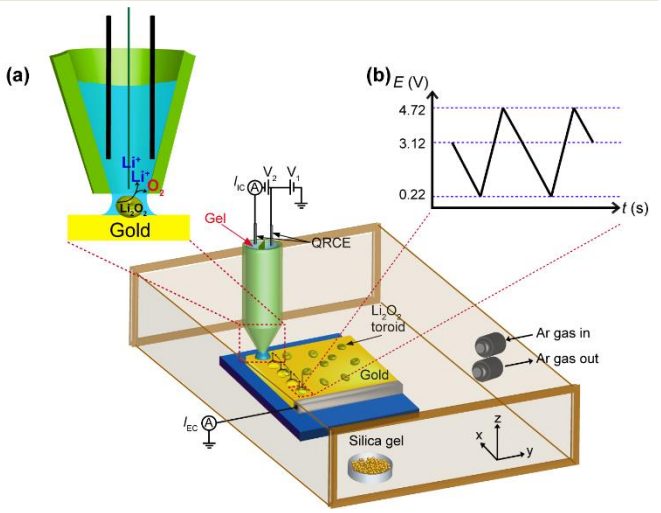

Fig. 2 (a) Schematic (not to scale) showing the key features of the SECCM environmental cell set-up for voltammetric electrochemical mapping measurements. (b) CV measurements at every pixel of a pre-defined scanned area.

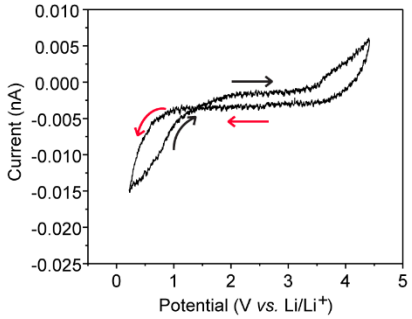

Fig. 3 A typical SECCM hopping CV of reduction of oxygen in gel polymer organic electrolyte containing 0.1 M $TBAPF_6$ and DMSO on the gold surface in argon filled environmental control cell. The CV is scanned from3.12 $\boldsymbol{V}_{\mathbf{Li/Li^+}}$ to 0.22 $\boldsymbol{V}_{\mathbf{Li/Li^+}}$ (negative direction) followed by scanning positively to 4.72 $\boldsymbol{V}_{\mathbf{Li/Li^+}}$.

Additionally, pixel-level CV analysis of the electrochemical response of any particular sites could be performed, as well as the average response from those pixels of particular surface character. The potential range allowed for the investigation of both the discharging and charging processes (eq. 1), with the forward process corresponding to discharge (reduction at the cathode) and the reverse reaction describing charging.[32-34]

The SECCM topographical image (Fig. 4a) highlights the locations of Li_2O_2 toroids (labelled regions 1 and 2) where the height of the surface is 1 – 1.2 µm above the background conformal layer. This is confirmed by Fig. 4b, which shows an FE-SEM image of the same area, obtained after SECCM imaging, where the meniscus footprints on the toroids match well to the SECCM topographical image. This coincidence between the location of toroids in the SECCM image (Fig. 4a) and FE-SEM is clearer in the magnified FE-SEM image (Fig. 4c) focusing on location 1 (Fig. 4a). The images in Fig. 4b and 4c also show that the size and shape of the meniscus were reasonably consistent on the substrate throughout the entire scanning procedure, confirming a similar local working electrode area at each pixel, so that the current-potential response at each pixel could be compared.

For an in-depth comparison of the Li_2O_2 toroids and the conformal Li_2O_2 layer, CV data were extracted (Fig. 4d), and averaged, from 4 individual pixels at each of the two distinct regions, according to results from the topographical image presented in Fig. 4a. During the first cathodic sweep of the cyclic voltammogram on the conformal layer, there was a very flat background and a wide potential window before solvent/electrolyte breakdown at extreme anodic and cathodic potentials.

Evidently the Li_2O_2 toroids are more active. In the first cathodic sweep, there is a small peak at 2.39 $\mathbf{V}_{\mathbf{Li/Li^+}}$ due to the discharge reaction (Fig. 4e), indicating a small amount of O_2 and Li^+ in the meniscus, from the electrodissolution of Li_2O_2 at the start of potential (3.12 $\mathbf{V}_{\mathbf{Li/Li^+}}$). Thereafter, the peak at *ca.* 1 V *vs*. Li/Li^+ is attributed to electrocatalyzed solvent breakdown.[32] During the second CV on the Li_2O_2 toroids, a relatively higher I_p at 2.39 $\mathbf{V}_{\mathbf{Li/Li^+}}$ appears (Fig. 4f) due to the more extensive electrodissolution of Li_2O_2 on the reverse (anodic) scan of the first sweep.

Electrochemical images at 2.39 $\mathbf{V}_{\mathbf{Li/Li^+}}$ on the cathodic scan (Fig. 4f) shows a strong contrast of electrochemical activity between the Li_2O_2 toroid and the Li_2O_2 layer. Further, the charging processes (oxidation) extracted from the video (at E_{app} = 3.59 $\mathbf{V}_{\mathbf{Li/Li^+}}$ and 4.12 $\mathbf{V}_{\mathbf{Li/Li^+}}$, Fig. 4g and 4h, respectively) illustrate the much higher electrochemical activity on Li_2O_2 toroids compared to the Li_2O_2 film. These results show that the Li_2O_2 oxidation occurs at a relatively lower overpotential (onset potential of 2.77 $\mathbf{V}_{\mathbf{Li/Li^+}}$) with a significantly high current generated (*ca*. 9 times increase in the peak current for the oxidation process) at the toroidal structure, compared to Li_2O_2 layered structure (onset potential of 3.25 $\mathbf{V}_{\mathbf{Li/Li^+}}$). Hence, toroidal Li_2O_2 structures boost the cell-charging capability of the cathode material. The low current magnitude at the Li_2O_2

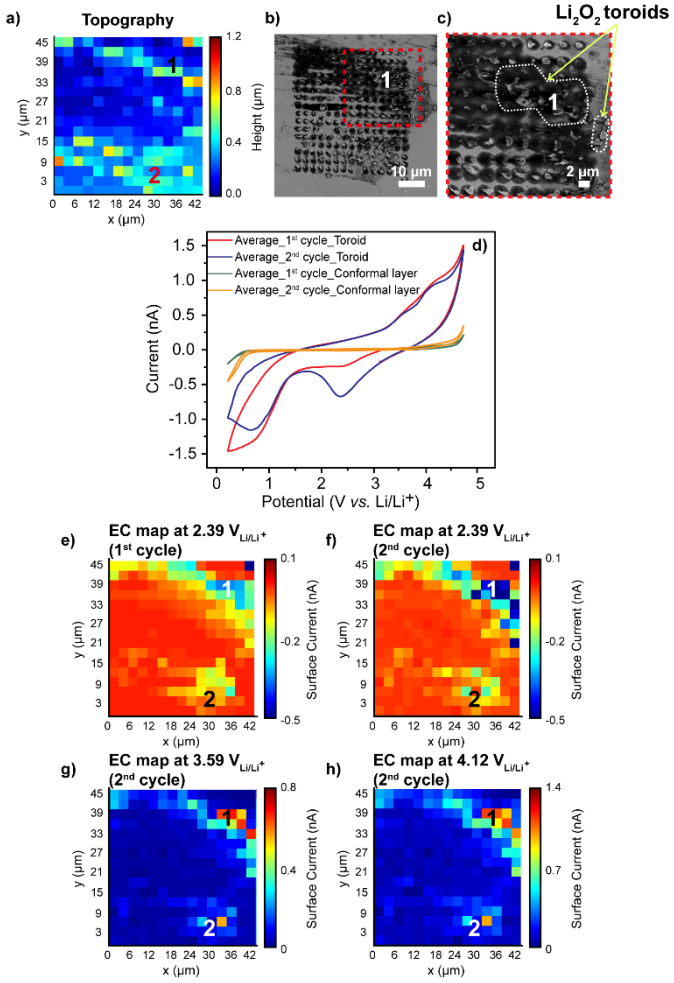

Fig. 4 (a) Topography measured simultaneously with the electrochemical measurements using voltammetric hopping mode SECCM in the Ar environmental chamber. (b) FE-SEM image after SECCM imaging showing the locations of the individual pixels. (c) Magnified FE-SEM image after SECCM imaging at region 1. (d) Averaged CVs (n = 4) for Li_2O_2 toroid (1st cycle (red); 2nd cycle (blue)) and Li_2O_2 layer (1st cycle (green); 2nd cycle (orange)). Electrochemical map of the Li_2O_2 modified gold substrate (conditions as Fig. S1, ESI†) at 2.39 $\mathbf{V}_{\mathbf{Li/Li^+}}$ for the cathodic scan direction on the (e) first and (f) second potential cycle. Electrochemical map different oxidation potential at (g) 3.59 $\mathbf{V}_{\mathbf{Li/Li^+}}$ and (h) 4.12 $\mathbf{V}_{\mathbf{Li/Li^+}}$ for the second cycle. Full movies can be found in ESI† Movie S1 and Movie S2 for the first and second cycle, respectively.

conformal layer, is most likely due to the poor electrical conductivity of the wide bandgap insulating Li_2O_2 layer, which impedes further charge transfer at the surface.[8-9, 35-37]

In summary, we have been able to compare the electrochemical characteristics of toroidal and conformal layer Li_2O_2 directly using a novel organic-gel based imaging probe deployed in an SECCM format. The unique gel polymer organic electrolyte probe has enabled localized CV measurements at a series of pixels in a pre-defined scanned area and, through the use of other microscopic techniques in parallel, has enabled detailed correlations of structure-activity. Notably, Li_2O_2 toroids are promising structures showing nearly an order of magnitude increase in the maximum oxidation and reduction current density, as compared to the conformal layer on the same surface.

There has been a great deal of interest in new techniques for the investigation of electrode processes in batteries,[38-40] however there have been relatively few reports on the use of nanoscale electrochemical probe redox mapping of battery materials. The studies herein add substantial new capability to SECCM, which has promise in revealing considerable information on battery electrodes[41] and electrocatalysts generally.[42-43] The use of a gel electrolyte in the SECCM probe will diversify the applications of this powerful technique.

P.R.U thanks the Royal Society for a Wolfson Research Merit Award and this work was, in part, supported by EPSRC through the MOAC DTC, Grant No. EP/F500378/1 (D.P.). A.B. acknowledges the Australian Government's Endeavour Fellowships and Scholarships Programme. M. Kang, L. Meng and S.P.E would like to thank the University of Warwick for funding through the award of Chancellor's International Scholarships. The authors thank Dr. Akichika Kumatani for fruitful discussions.

Notes and references

1 Y. C. Lu, Z. Xu, H. A. Gasteiger, S. Chen, K. Hamad-Schifferli and Y. Shao-Horn, *J. Am. Chem. Soc.*, 2010, **132**, 12170-12171.
2 R. Black, B. Adams and L. F. Nazar, *Adv. Energ. Mater.*, 2012, **2**, 801-815.
3 P. G. Bruce, S. A. Freunberger, L. J. Hardwick and J. M. Tarascon, *Nat. Mater.*, 2012, **11**, 19-29.
4 Y.-C. Lu, B. M. Gallant, D. G. Kwabi, J. R. Harding, R. R. Mitchell, M. S. Whittingham and Y. Shao-Horn, *Energ. & Environ. Sci.*, 2013, **6**, 750-768.
5 A. Basile, A. I. Bhatt and A. P. O'Mullane, *Nat. Commun.*, 2016, **7**.
6 J. Christensen, P. Albertus, R. S. Sanchez-Carrera, T. Lohmann, B. Kozinsky, R. Liedtke, J. Ahmed and A. Kojic, *J. Electrochem. Soc.*, 2012, **159**, R1-R30.
7 G. Girishkumar, B. McCloskey, A. C. Luntz, S. Swanson and W. Wilcke, *J. Phys. Chem. Lett.*, 2010, **1**, 2193-2203.
8 A. C. Luntz, V. Viswanathan, J. Voss, J. B. Varley, J. K. Norskov, R. Scheffler and A. Speidel, *J. Phys. Chem. Lett.*, 2013, **4**, 3494-3499.
9 M. D. Radin and D. J. Siegel, *Energ. & Environ. Sci.*, 2013, **6**, 2370-2379.
10 M. M. Ottakam Thotiyl, S. A. Freunberger, Z. Peng and P. G. Bruce, *J. Am. Chem. Soc.*, 2013, **135**, 494-500.
11 Y. Qiao and S. Ye, *J. Phys. Chem. C*, 2016, **120**, 8033-8047.
12 R. R. Mitchell, B. M. Gallant, Y. Shao-Horn and C. V. Thompson, *J. Phys. Chem. Lett.*, 2013, **4**, 1060-1064.
13 L. Danis, S. M. Gateman, C. Kuss, S. B. Schougaard and J. Mauzeroll, *ChemElectroChem*, 2017, **4**, 6-19.
14 C. Liu and S. Ye, *J. Phys. Chem. C*, 2016, **120**, 25246-25255.
15 B. D. Adams, C. Radtke, R. Black, M. L. Trudeau, K. Zaghib, L. F. Nazar, *Energ. & Environ. Sci.*, 2013, **6**, 1772-1778.
16 X. Zhang, X.-G. Wang, Z. Xie, Z. Zhou, *Green Energ. & Environ.*, 2016, **1**, 4-17.
17 L. Wang, Y. Zhang, Z. Liu, L. Guo, Z. Peng, *Green Energ. & Environ.*, 2017, **2**, 186-203.
18 N. B. Aetukuri, B. D. McCloskey, J. M. Garcia, L. E. Krupp, V. Viswanathan and A. C. Luntz, *Nat. Chem.*, 2015, **7**, 50-56B.
19 D. McCloskey, A. Speidel, R. Scheffler, D. C. Miller, V. Viswanathan, J. S. Hummelshoj, J. K. Norskov and A. C. Luntz, *J. Phys. Chem. Lett.*, 2012, **3**, 997-1001.
20 Z. Q. Peng, S. A. Freunberger, Y. H. Chen and P. G. Bruce, *Science*, 2012, **337**, 563-566.
21 Y. Shao, S. Park, J. Xiao, J.-G. Zhang, Y. Wang and J. Liu, *ACS Catal.*, 2012, **2**, 844-857.
22 Y. Zhang, X. Zhang, J. Wang, W. C. McKee, Y. Xu and Z. Peng, *J. Phys. Chem. C*, 2016, **120**, 3690-3698.
23 L. Johnson, C. M. Li, Z. Liu, Y. H. Chen, S. A. Freunberger, P. C. Ashok, B. B. Praveen, K. Dholakia, J. M. Tarascon and P. G. Bruce, *Nat. Chem.*, 2014, **6**, 1091-1099.
24 J. Yang, D. Zhai, H.-H. Wang, K. C. Lau, J. A. Schlueter, P. Du, D. J. Myers, Y.-K. Sun, L. A. Curtiss and K. Amine, *Phys. Chem. Chem. Phys.*, 2013, **15**, 3764-3771.
25 C.-H. Chen, L. Jacobse, K. McKelvey, S. C. S. Lai, M. T. M. Koper and P. R. Unwin, *Anal. Chem.*, 2015, **87**, 5782-5789.
26 J. C. Byers, A. G. Güell and P. R. Unwin, *J. Am. Chem. Soc.*, 2014, **136**, 11252-11255.
27 B. D. B. Aaronson, J. Garoz-Ruiz, J. C. Byers, A. Colina and P. R. Unwin, *Langmuir*, 2015, **31**, 12814-12822.
28 B. D. B. Aaronson, S. C. S. Lai and P. R. Unwin, *Langmuir*, 2014, **30**, 1915-1919.
29 A. M. Stephan, *Eur. Polym. J.*, 2006, **42**, 21-42.
30 J. Y. Song, Y. Y. Wang and C. C. Wan, *J. Power Sources*, 1999, **77**, 183-197.
31 D. Xu, Z. L. Wang, J. J. Xu, L. L. Zhang and X. B. Zhang, *Chem. Commun.*, 2012, **48**, 6948-6950.
32 C. O. Laoire, S. Mukerjee, K. M. Abraham, E. J. Plichta and M. A. Hendrickson, *J. Phys. Chem. C*, 2010, **114**, 9178-9186.
33 T. Ogasawara, A. Debart, M. Holzapfel, P. Novak and P. G. Bruce, *J. Am. Chem. Soc.*, 2006, **128**, 1390-1393.
34 C. O. Laoire, S. Mukerjee, K. M. Abraham, E. J. Plichta and M. A. Hendrickson, *J. Phys. Chem. C*, 2009, **113**, 20127-20134.
35 V. Viswanathan, K. S. Thygesen, J. S. Hummelshoj, J. K. Norskov, G. Girishkumar, B. D. McCloskey and A. C. Luntz, *J. Chem. Phys.*, 2011, **135**, 214704.
36 P. Albertus, G. Girishkumar, B. McCloskey, R. S. Sanchez-Carrera, B. Kozinsky, J. Christensen and A. C. Luntz, *J. Electrochem. Soc.*, 2011, **158**, A343-A351.
37 M. D. Radin, F. Tian and D. J. Siegel, *Energ. & Environ. Sci.*, 2013, **6**, 2370-2379.
38 R. Huang and Y. Ikuhara, *Curr. Opin. Solid State Mater. Sci.*, 2012, **16**, 31-38.
39 W. C. Chueh, F. El Gabaly, J. D. Sugar, N. C. Bartelt, A. H. McDaniel, K. R. Fenton, K. R. Zavadil, T. Tyliszczak, W. Lai and K. F. McCarty, *Nano Lett.*, 2013, **13**, 866-872.
40 R. Baddour-Hadjean and J.-P. Pereira-Ramos, *Chem. Rev.*, 2010, **110**, 1278-1319.
41 Y. Takahashi, A. Kumatani, H. Munakata, H. Inomata, K. Ito, K. Ino, H. Shiku, P. R. Unwin, Y. E. Korchev, K. Kanamura and T. Matsue, *Nat. Commun.*, 2014, **5**.
42 C. L. Bentley, M. Kang and P. R. Unwin, *J. Am. Chem. Soc.*, 2017, **139**, 16813-16821.
43 R. G. Mariano, K. McKelvey, H. S. White and M. W. Kanan, *Science*, 2017, **358**, 1187-1191.

